LQR Control of an All-Wheel Drive Vehicle Considering Variable Input Constraint

Hojin Jung, Dohyun Jung and Seibum B. Choi, *Member, IEEE*

***Abstract*—This paper suggests a model-based controller for an all-wheel drive (AWD) vehicle using a novel vehicle dynamics model. Recently, an active type of AWD system that automatically controls the clutch engagement force of the transfer case has become popular. However, its performance has been limited by its rule-based controller, which necessitates the development of a model-based controller. Although the bicycle model has been most widely adopted for upper level controller of vehicle control systems, it is not appropriate for AWD controllers because the model does not have a direct relationship between the states and control inputs. In this sense, this study adopted a tire force based-full car model for the AWD controller. The clutch engagement force limit, which varies depending on the current engagement state, was calculated systematically by considering multiple dynamic behavior that is inherent in AWD vehicle, and was used as a valid value for input limit in linear quadratic regulator (LQR) control algorithm. For the real-time application of the designed controller, only data obtained from the controller area network (CAN) of production vehicles were used. Then, performance of proposed controller was validated through vehicle experiments that included scenarios of both longitudinal and lateral movements.**

***Index Terms*—All-wheel drive, LQR control, constrained system, torque on demand transfer case, vehicle dynamics model**

I. Introduction

OVER the past few years, several types of vehicle dynamics control systems have been constantly developed to meet increasing demands for vehicle safety and performance [1]–[3]. Among them, all-wheel drive (AWD) systems, which transfer the driving torque through a transfer case to all the wheels, have proven effective for improving vehicle performance in aspect of the cost-to-benefit ratio; thus, the market share of AWD vehicles has steadily increased [4]. Unlike braking torque-based vehicle dynamics control systems, e.g., anti-lock brake (ABS) and electronic stability control (ESC), the activation of an AWD system can relieve driver discomfort because it does not generate braking torque. Therefore, AWD system is activated first among other vehicle dynamics systems when unstable or undesirable motions are detected, and taking advantage of AWD system when it is needed can enhance the vehicle's overall performance. One type of active AWD system, a transfer case with multiple wet-clutches and an electro-hydraulic actuator, has two characteristics. First, the wet clutch system can endure clutch slip for a certain amount of time, which occurs when the clutch is in slipping state. Second, in contrast to a selective four-wheel drive (4WD) system, which is controlled manually by the driver, the electro-hydraulic actuator can automatically command the engagement force of the transfer case by constantly observing the motions of the vehicle. Therefore, an AWD vehicle equipped with this type of transfer case can determine the amount of torque that is distributed between the main-drive shaft and sub-drive shaft at ratios from 0:100 to 50:50.

Manuscript received October 30, 2018; revised , 2018. This work was supported in parts by the National Research Foundation of Korea grant funded by the Korea government (MSIP) (No. 2017R1A2B4004116).

Hojin Jung and Seibum B. Choi are with the Department of Mechanical Engineering, Korea Advanced Institute of Science and Technology (KAIST), Daejeon 34141, Korea (email:bourne@kaist.ac.kr; sbchoi@kaist.ac.kr). Dohyun Jung is with the Driving & Safety System R&D Center, Korea Automotive Technology Institute (KATECH), Cheonan 31214, Korea (email:dhjung@katech.re.kr)

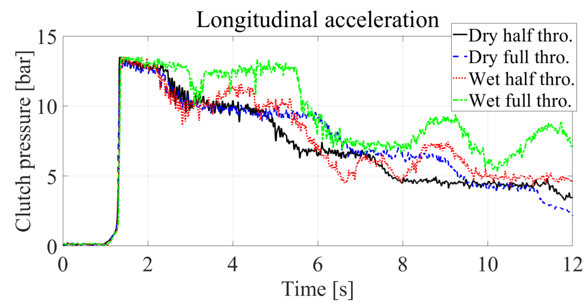

Fig. 1. Clutch pressure of a rule-based controller during longitudinal acceleration in an AWD vehicle depending on road conditions and throttle inputs.

An active type AWD system is more advantageous than a selective 4WD system because its variable torque distribution can control the motion of the vehicle in a more desirable way. However, its control algorithm has not been treated systematically. The rule-based controller used in a commercially produced transfer case generates clutch command inputs by referencing some vehicle indices, e.g., throttle position and transmission output torque. Fig. 1 shows the clutch pressure of a rule-based controller while a vehicle is accelerating in a straight line in several road conditions and throttle positions. Here, the rule-based controller demonstrated very typical actuation responses in all cases, i.e., slowly decreasing the clutch pressure of the transfer case from full engagement pressure. In addition, the rule-based controller did not perform effectively by having similar actuation responses regardless of road conditions. Therefore, a model-based controller design should be advanced for the maximized performance of active-type AWD vehicles in all driving scenarios.

There have been a few approaches to designing controllers for other types of AWD vehicles than the one addressed in this study. Kim et al. [5] suggested a transfer case and torque vectoring controller with the least generation of additional traction force. Osborn and Shim [6] suggested the map-based control of an in-wheel motor vehicle using a matrix that represents the relationship between input and output parameters. Croft-White and Harrison [7] proposed a torque vectoring control scheme for an AWD vehicle that applies a sideslip angle minimization strategy. Han et al. [8] suggested sliding mode control of hybrid 4WD system by finding desired wheel slip ratio simultaneously. However, these approaches have not paid much attention to selecting a proper vehicle dynamic model for controller design.

Generally, the previous approaches of designing model-based vehicle dynamics controllers were mostly based on the bicycle model [9]–[12]. However, the bicycle model does not have a direct relationship between the clutch engagement force of a transfer case and the vehicle motion states, making it inappropriate to apply to an AWD controller. To design an advanced model-based controller, this study adopted a planar full-car dynamic model especially for an AWD vehicle that represents the direct relationship between the clutch engagement force of the transfer case and the motion states.

As a general rule, vehicle owns highly nonlinear dynamic characteristic, especially in view of lateral behavior that has both stable equilibrium point and unstable equilibrium point in phase portrait of yaw rate vs. sideslip angle [13]. Also, due to the highly lagged response of the transfer case actuator (see $t = 1 - 2s$ in Figure 10e), extremely small phase margin is allowed for feedback controller design, which makes it difficult to apply linear system control theory such as H_∞ control [14]. Another noteworthy issue is that there exists the constrained condition of clutch engagement force in an AWD vehicle. In contrast to a vehicle that is equipped with an in-wheel motor, a vehicle that is equipped with a transfer case has the constraint of maximum transferable torque, owing to the mechanical characteristic of its clutch. When the clutch is in a slipping state, the transferred torque is proportional to the engagement force. When the clutch is in a lock-up state, the transferred torque is not related to the engagement force but, rather, is determined by the transmission output torque, load on each drive shaft, and the parameters of the vehicle specifications. In order to consider system constraints in the optimal control, model predictive control (MPC) has been studied widely [15]–[17] and has been adopted in other studies of vehicle dynamics controller design [18]–[22]. MPC takes advantage of a system dynamics to predict the future system response and to accordingly determine the best control action by explicitly considering the system constraints in the specified performance index, such as the cost function.

Although MPC is beneficial, its computational burden of calculating the control input makes it difficult to apply in a real-time controller. Furthermore, the performance of MPC is greatly affected by the solvers selected [23], [24]. To avoid these issues, this paper suggests an linear quadratic regulator (LQR) controller, in which input constraint is decoupled in the performance criterion. In the LQR control formulation, exact range of clutch engagement force constraint was systemically considered by adopting the concept of variable input constraint that can be calculated by summing two different input constraints multiplied by current model probabilities depending on vehicle dynamic models, which is obtained from interacting multiple model (IMM) filter.

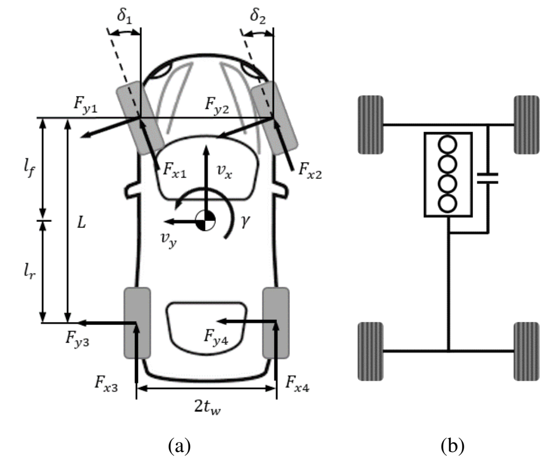

Fig. 2. Planar full car model and AWD driveline layout. (a) States and parameters related to the vehicle. (b) Driveline of AWD test vehicle.

It is commonly understood that an AWD system can enhance the longitudinal acceleration performance on off-road, slippery road, and hilly conditions. However, AWD system also helps the vehicle to provide a stable response in the lateral direction. This study focuses on an AWD controller that considers both the longitudinal acceleration performance and lateral stability of the vehicle. Along with vehicle longitudinal slip ratio and yaw rate, which are basic targets for designing a practical controller, longitudinal and lateral tire forces were used as additional targets to fully utilize the adopted AWD vehicle dynamics model.

The organization of this paper is as follows. The vehicle dynamics models for the controller design are described in Section II. Section III describes the selection of controller target states. Section IV describes how to calculate the engagement force limit. Section V describes the control algorithm for an AWD vehicle. Section VI explains the experimental setup of the test vehicle. Finally, Section VII provides the experimental results that validate the advantages of the suggested controller.

II. System Model

Depending on the engagement state of the transfer case clutch, i.e., whether the clutch is slipping or in the lock-up state, the AWD vehicle dynamic model can be different. Fig. 2a illustrates the planar full car model that includes vehicle motion states, tire forces and parameters.

A. AWD Wheel Dynamics Model Set

1) Slipping state: When the transfer case clutch is in the slipping state, AWD system can actively control the amount of torque transferred to the front shaft by adjusting the engagement force. Referring to the wheel dynamic model presented in [25], the dynamic equation of motion for the wheel can be modified as follows:

$$I_w\dot{\omega}_i = \mu_c r_c n F_c \frac{i_f}{2} - T_{bi} - R_e F_{xi} - R_e R_r F_{zi}, i = 1, 2 \quad (1)$$

$$I_w\dot{\omega}_i = \left(T_t - \mu_c r_c n F_c\right)\frac{i_r}{2} - T_{bi} - R_e F_{xi} - R_e R_r F_{zi} \quad i = 3,4 \tag{2}$$

where $\omega_i, i_f, i_r, F_c, \mu_c, r_c, I_w, n,$ and R_e are the wheel angular velocity at each wheel, front final reduction gear ratio, rear final reduction gear ratio, clutch engagement force of the transfer case, clutch friction coefficient of the transfer case, effective clutch plate radius of the transfer case, wheel moment of inertia, number of clutch plates and effective wheel radius, respectively. $T_{bi}, R_r, F_{xi},$ and F_{zi} are the braking torque, rolling resistance, longitudinal traction force, and vertical force at each wheel, respectively. T_t is the transmission output torque that can be easily obtained from the controller area network (CAN) signals for engine torque and gear ratio.

2) Lock-up state: When the transfer case clutch is in a lock-up state, AWD system cannot actively control the amount of torque transferred to the front shaft. This means that the front-to-rear torque distribution ratio is determined not by the clutch engagement force, but by the external conditions. Then, the dynamic equation of motion for the wheel is expressed as follows:

$$\begin{aligned} I_w\dot{\omega}_i =& \frac{\mu_f\left(gl_r - a_x h\right)}{\mu_f\left(gl_r - a_x h\right) + \mu_r\left(gl_f + a_x h\right)}\frac{T_t i_f}{2} \\ & - T_{bi} - R_e F_{xi} - R_e R_r F_{zi}, i = 1,2 \end{aligned} \tag{3}$$

$$\begin{aligned} I_w\dot{\omega}_i =& \frac{\mu_f\left(gl_f + a_x h\right)}{\mu_f\left(gl_r - a_x h\right) + \mu_r\left(gl_f + a_x h\right)}\frac{T_t i_r}{2} \\ & - T_{bi} - R_e F_{xi} - R_e R_r F_{zi}, i = 3,4 \end{aligned} \tag{4}$$

where $\mu_f, \mu_r, a_x, g, h, l_f,$ and l_r are the front road friction coefficient, rear road friction coefficient, longitudinal acceleration, gravitational acceleration, and height from the ground to the vehicle's center of gravity (CG), distance from the vehicle's CG to the front axle, and distance from the vehicle's CG to the rear axle, respectively. However, the information of μ_f and μ_r is not easy to be obtained in a real-time only with in-vehicle sensors, which reduces the practicality of (3) and (4). In general, vehicle usually drives on homogeneous road surface. So by assuming μ_f and μ_r are the same, the above expression can be simplified as follows:

$$I_w\dot{\omega}_i = \left(\frac{l_r}{L} - \frac{a_x h}{gL}\right)\frac{T_t i_f}{2} - T_{bi} - R_e F_{xi} - R_e R_r F_{zi} \quad i = 1,2 \tag{5}$$

$$I_w\dot{\omega}_i = \left(\frac{l_f}{L} + \frac{a_x h}{gL}\right)\frac{T_t i_f}{2} - T_{bi} - R_e F_{xi} - R_e R_r F_{zi} \quad i = 3,4 \tag{6}$$

where L is wheelbase length. This study adopted (5) and (6) as the AWD wheel dynamics model for the lock-up state to delete the trivial parameters.

B. Tire-Road Relation Model Set

1) Steady Tire Model: Among several tire-road relation models in previous studies, the Dugoff tire model has been mostly adopted to estimate individual tire lateral force. Although the Dugoff model is quite simple compared to other tire models, it is still not appropriate for real-time controller application due to road friction coefficient parameter that must be identified in advance. Generally, the main reason to include the tire model in the vehicle dynamics is to consider the nonlinear tire effect caused by both the vertical load transfer and vehicle sideslip angle. This paper adopted a simple tire model that addresses the nonlinear effect in the vehicle dynamics to avoid all of the above drawbacks. The steady model of lateral tire force is described as follows [26]:

$$\begin{aligned} \bar{F}_y =& C_1\left(1 + k_1\frac{F_{zi} - F_{zi,n}}{F_{zi,n}}\right)\alpha \\ & + C_2\left(1 + k_2\frac{F_{zi} - F_{zi,n}}{F_{zi,n}}\right)\alpha^2 \end{aligned} \tag{7}$$

where $\bar{F}_y$ is the lateral tire force in the steady-state, C_1 is the cornering stiffness and C_2 is the auxiliary cornering stiffness. k_1 and k_2 are adjustment factors. $F_{zi,n}$ is the nominal vertical load without including both the longitudinal and lateral acceleration effects. In this study, F_{zi} is calculated using the equation presented in [27].

C. Dynamic Tire Model

A first-order dynamic model can be applied as follows, to address the lagging behavior of the tire force generation:

$$\frac{\sigma}{v_x}\dot{F}_{yi} + F_{yi} = \bar{F}_{yi}, i = 1,2,3,4 \tag{8}$$

Here, σ is the relaxation length which consists of two tire parameters as follows:

$$\sigma = \frac{C_\alpha}{K_L} \tag{9}$$

D. AWD Vehicle Dynamics Model for Controller Application

Selecting the proper vehicle dynamic model for controller design is important as it is closely related to the performance of the controller. However, the bicycle (single-track) model is inappropriate for an AWD controller because the relationship between the clutch engagement force of transfer case (control input) and the states is not explicitly represented [9], [12], [28], [29]. Because the transfer case control input term appears in the wheel dynamics model, it should be included in the entire model for control applications. Furthermore, the control input and other states are related to each other through the tire force states, so it is necessary to construct an AWD vehicle dynamics model based on the tire forces. Therefore, the following nonlinear vehicle dynamics model, which explicitly represents the relationship between the control input and states, was adopted for the control application:

$$\dot{\mathbf{x}}(t) = f\left(\mathbf{x}(t), u(t)\right) \tag{10}$$

The state vector $\mathbf{x}(t)$ consists of the longitudinal velocity, the lateral velocity, the yaw rate, the four wheel angular velocities, and the tire forces:

$$\begin{aligned} \mathbf{x}(t) &= \left[v_x, v_y, \gamma, \boldsymbol{\omega}_{[1\times4]}, \mathbf{F}_{[1\times8]}\right]^T \\ &= \left[x_1, x_2, \ldots, x_{15}\right]^T \end{aligned} \tag{11}$$

Here, $\boldsymbol{\omega}_{[1\times4]}$ and $\mathbf{F}_{[1\times8]}$ are the wheel angular velocity vector and the tire force vector, respectively:

$$\boldsymbol{\omega}_{[1\times4]} = [\omega_1, \omega_2, \omega_3, \omega_4] \tag{12}$$

$$\mathbf{F}_{[1\times8]} = [F_{x1}, F_{x2}, F_{x3}, F_{x4}, F_{y1}, F_{y2}, F_{y3}, F_{y4}] \tag{13}$$

The input $u(t)$ is the clutch engagement force F_c. The particular function f of AWD vehicle dynamic model can be expressed as follows:

$$\begin{cases} f_1 = \frac{1}{m}\{(x_8+x_9)\cos(\delta_f) - (x_{12}+x_{13})\sin(\delta_f) \\ \quad +x_{10}+x_{11} - \frac{1}{2}\rho_{air}C_d A x_1^2\} + x_2 x_3 \\ f_2 = \frac{1}{m}\{(x_8+x_9)\sin(\delta_f) + (x_{12}+x_{13})\cos(\delta_f) \\ \quad +x_{14}+x_{15}\} - x_1 x_3 \\ f_3 = \frac{1}{I_z}[l_f\{(x_8+x_9)\sin(\delta_f) + (x_{12}+x_{13})\cos(\delta_f)\} \\ \quad +t_w\{(-x_8+x_9)\cos(\delta_f) + (x_{12}-x_{13})\sin(\delta_f) \\ \quad -x_{10}+x_{11}\} - l_r(x_{14}+x_{15})] \\ f_4 = \frac{1}{I_w}\left(\mu_c r_c n u(t)\frac{i_f}{2} - T_{b1} - R_e x_8 - R_e R_r F_{z1}\right) \\ f_5 = \frac{1}{I_w}\left(\mu_c r_c n u(t)\frac{i_f}{2} - T_{b2} - R_e x_9 - R_e R_r F_{z2}\right) \\ f_6 = \frac{1}{I_w}\left\{(T_t - \mu_c r_c n u(t))\frac{i_r}{2} - T_{b3} - R_e(x_{10} \right. \\ \quad \left. -R_r F_{z3})\right\} \\ f_7 = \frac{1}{I_w}\left\{(T_t - \mu_c r_c n u(t))\frac{i_r}{2} - T_{b4} - R_e(x_{11} \right. \\ \quad \left. -R_r F_{z4})\right\} \\ f_8 = 0,\ f_9 = 0,\ f_{10} = 0,\ f_{11} = 0 \\ f_{12} = \frac{x_1}{\sigma}\left(-x_{12}+\bar{F}_{y1}\right),\ f_{13} = \frac{x_1}{\sigma}\left(-x_{13}+\bar{F}_{y2}\right) \\ f_{14} = \frac{x_1}{\sigma}\left(-x_{14}+\bar{F}_{y3}\right),\ f_{15} = \frac{x_1}{\sigma}\left(-x_{15}+\bar{F}_{y4}\right) \end{cases} \tag{14}$$

where $\rho_{air}, C_d, A, \delta_f$, and σ are the density of air, air drag coefficient, front cross-sectional area, steered angle of front wheel, and tire relaxation length, respectively. The governing equations of motion and tire force were obtained following the information in Fig. 2a.

III. Target States Selection For Controller

A. Longitudinal Direction

1) Wheel angular velocity: It has been empirically proven that the tire-road friction coefficient is highly related to the wheel slip ratio [30], [31]. Fig. 3 shows the typical adhesion coefficient characteristics that are obtained from the Burckhardt's tire friction model. Except for extraordinary cases (e.g., dry cobblestone), the tire-road friction has a peak value at a certain wheel slip ratio for each road surface. Although each surface has a slightly different peak point, it was assumed that the desired wheel slip ratio was already known because the peak points are clustered at certain boundaries, and the

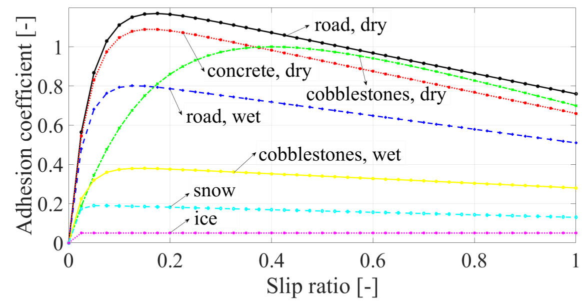

Fig. 3. Typical adhesion coefficient characteristics.

purpose of this study was the control, not the desired target value generation. In this study, $\lambda_d = 0.15$ was used as the desired slip ratio.
Using the information of the wheel angular velocity and the estimation of the vehicle velocity [32], [33], the wheel slip ratio can be obtained. Therefore, wheel slip-based control in the longitudinal direction is feasible without requiring additional sensors. Wheel slip ratio, λ, is defined as follows:

$$\lambda = \begin{cases} \dfrac{R_e\omega - v_x}{R_e\omega}, & \text{acceleration} \\ \dfrac{v_x - R_e\omega}{v_x}, & \text{deceleration} \end{cases} \tag{15}$$

In the case of acceleration, the desired vehicle longitudinal angular velocity, ω_d, is obtained as follows:

$$\omega_d = \frac{v_x}{R_e(1-\lambda_d)} \tag{16}$$

2) Longitudinal tire force: To maximize the effectiveness of the tire force-based vehicle dynamic model, the tire force state was also used as a target. The desired longitudinal tire force can be determined from the allowable traction force as follows:

$$F_{xid} = \mu_p F_{zi}, i = 1,2,3,4 \tag{17}$$

where μ_p is the peak of the road friction coefficient.

B. Lateral Direction

1) Yaw rate: As for the targets of the lateral motion states, the yaw rate, γ, and sideslip angle, β, have been selectively used in previous studies. Yaw rate has proven to be a practical state and has been widely adopted because the yaw rate sensor is built into the vehicle. Although control based on the sideslip angle can enhance the lateral response of the vehicle, not only for stability but also for performance, it requires an additional estimator or sensor [2], [34]. Further, an AWD system distributes the engine torque only between the front and rear, not from side to side, which limits the dynamic responsiveness in the lateral direction. Therefore, only the yaw rate was used as a target for the lateral motion states.
Desired yaw rate, γ_d, which indicates the vehicle is in steady-state cornering is expressed as follows:

$$\gamma_d = \operatorname{sgn}(\delta_f)\max\left(\left|\frac{v_x\delta_f}{L + \frac{mv_x^2}{L}\left(\frac{l_r}{C_f} - \frac{l_f}{C_r}\right)}\right|, \left|\frac{\mu g}{v_x}\right|\right) \tag{18}$$

where C_f and C_r are the front and rear cornering stiffnesses, respectively.

2) Lateral tire force: The desired lateral tire force can be determined from the condition of steady-state cornering as follows:

$$F_{yid} = \frac{F_{zi}}{F_{z1}+F_{z2}}\frac{l_f}{L}mv_x\gamma_d, i=1,2 \tag{19}$$

$$F_{yid} = \frac{F_{zi}}{F_{z3}+F_{z4}}\frac{l_r}{L}mv_x\gamma_d, i=3,4 \tag{20}$$

Here, it is noteworthy that the distribution between left and right was determined to follow the current vertical load distribution.

IV. Engagement Force Constraint

An AWD vehicle has a constraint that is originates from its clutch system characteristics, and it is noteworthy that this constraint is affected by the engagement state of the clutch. Thus, it should be considered when designing a controller to enhance its effectiveness. In the lock-up state, the amount of driving torque distributed to the front and rear wheels is no longer determined by the clutch engagement force, so that the occurrence of additional engagement force cannot affect the driving motion of the vehicle. Therefore, the controller should be designed to have its control input upper-bounded by the engaging force that transitions the vehicle into a lock-up state. However, it is impossible to determine the lock-up state and slipping state exactly, because there exists not only noise and the uncertainty of measurement accuracy in the in-vehicle sensors, but also the indefinite information of an external factor, e.g., the road friction coefficient that determines the external load of each shaft. Therefore, by applying the current probability of each model obtained through the interacting multiple model (IMM) filter-based AWD vehicle states estimator [32], the allowable engagement force limit can be calculated. Here, it was assumed that front and rear final reduction gear ratio and front and rear wheel radius are same. When an AWD vehicle drives on a homogeneous road surface while the transfer case clutch is in the fully locked-up state, the clutch engagement force is bounded as follows (see (5)):

$$0 \le F_c \le \left(\frac{l_r}{L} - \frac{a_x}{g}\frac{h}{L}\right)\frac{T_t}{\mu_c r_c n} \tag{21}$$

When an AWD vehicle drives on a random road surface while the transfer case clutch is in the slipping state, the clutch engagement force is bounded as follows:

$$0 \le F_c \le \frac{T_t}{\mu_c r_c n} \tag{22}$$

By integrating the above two constraints with the model probability, the constraint of clutch engagement force is expressed as follows:

$$0 \le F_c \le \left(\frac{l_r}{L} - \frac{a_x}{g}\frac{h}{L}\right)\frac{T_t}{\mu_c r_c n}p_1 + \frac{T_t}{\mu_c r_c n}p_2 \tag{23}$$

where p_1 and p_2 are the probabilities of the lock-up state and slipping state, respectively.

V. Controller Design

Linearization was conducted by taking the partial derivative of equation (10). Then, the following state-form was obtained:

$$\dot{\mathbf{x}}(t) = A_l\mathbf{x}(t) + B_l u(t) + E_l \tag{24}$$

where A_l, B_l and E_l are defined in (28)–(30).

A. Control Algorithm

Given the process model and current states, the suggested control algorithm calculates a set of optimal inputs that minimize the cost function over a predetermined prediction time horizon at each step. Then, only the first input in the set of optimal inputs is used, because a set of optimal inputs is newly obtained in each step with the updated state values. In order to reduce the calculation burden and avoid using a solver, this study adopted LQR control. Also, the input constraint was decoupled from the cost function and considered in the final step. To formulate the LQR problem, a discretized form of the process model is required. For LQR-based AWD controller design, the tire force-based AWD vehicle dynamic model (24) was discretized using a zero-order hold as follows:

$$\mathbf{x}_{k+1} = A_k\mathbf{x}_k + B_k u_k + E_k \tag{25}$$

Then, the cost function of the MPC in quadratic form is defined as follows:

$$\begin{aligned} J\left(\mathbf{x}_k, \mathbf{U}(k)\right) = \sum_{i=0}^{N-1} \big\{ &(\mathbf{x}_{k+i} - \mathbf{x}_{d,k+i})^T Q (\mathbf{x}_{k+i} - \mathbf{x}_{d,k+i}) \\ &+ u_{k+i}^T R u_{k+i} \big\} + (\mathbf{x}_{k+N} - \mathbf{x}_{d,k+N})^T P (\mathbf{x}_{k+N} - \mathbf{x}_{d,k+N}) \end{aligned} \tag{26}$$

where

$$\mathbf{U}(k) = [u_k, u_{k+1}, \dots, u_{k+N-1}]^T \tag{27}$$

The predicted state sequence obtained by the discretized process model (25) with the input sequence $U(k)$ can be expressed as:

$$\mathbf{X}(k) = L^x\mathbf{x}_k + L^u\mathbf{U}(k) + L^e \tag{31}$$

where

$$\mathbf{X}(k) = \begin{bmatrix} \mathbf{x}_{k+1} \\ \mathbf{x}_{k+2} \\ \vdots \\ \mathbf{x}_{k+N} \end{bmatrix}, L^x = \begin{bmatrix} A_k \\ A_k^2 \\ \vdots \\ A_k^N \end{bmatrix},$$

$$L^u = \begin{bmatrix} B_k & 0 & \cdots & \cdots & 0 \\ A_kB_k & B_k & 0 & \cdots & 0 \\ \vdots & \vdots & \ddots & & \vdots \\ \vdots & \vdots & & \ddots & \vdots \\ A_k^{N-1}B_k & A_k^{N-2}B_k & \cdots & \cdots & B_k \end{bmatrix},$$

$$L^e = \begin{bmatrix} E_k \\ A_kE_k + E_k \\ \vdots \\ A_k^{N-1}E_k + \cdots + E_k \end{bmatrix}$$

$$
A_l = \left[\begin{array}{cccccccc}
-\frac{\rho_{air}C_dA}{m}x_1 & x_3 & x_2 & & \frac{\cos(\delta_f)}{m} & \frac{\cos(\delta_f)}{m} & \frac{1}{m} & \frac{1}{m} \\
-x_3 & 0 & -x_1 & \mathbf{0}_{3\times4} & \frac{\sin(\delta_f)}{m} & \frac{\sin(\delta_f)}{m} & 0 & 0 \\
0 & 0 & 0 & & \frac{l_f\sin(\delta_f)-t_w\cos(\delta_f)}{I_z} & \frac{l_f\sin(\delta_f)+t_w\cos(\delta_f)}{I_z} & -\frac{t_w}{I_z} & \frac{t_w}{I_z} \\
\hline
\multicolumn{4}{c}{\mathbf{0}_{4\times7}} & \multicolumn{4}{c}{-\frac{R_e}{I_w}\cdot\mathbf{I}_{4\times4}} \\
\hline
\multicolumn{8}{c}{\mathbf{0}_{4\times11}} \\
\hline
\frac{-x_{12}+\bar{F}_{y1}}{\sigma} & 0 & 0 & 0 & & & & \\
0 & \frac{-x_{13}+\bar{F}_{y2}}{\sigma} & 0 & 0 & \multicolumn{4}{c}{\mathbf{0}_{4\times7}} \\
0 & 0 & \frac{-x_{14}+\bar{F}_{y3}}{\sigma} & 0 & & & & \\
0 & 0 & 0 & \frac{-x_{15}+\bar{F}_{y4}}{\sigma} & & & &
\end{array}\right.
$$

$$
\left.\begin{array}{cccc}
-\frac{\sin(\delta_f)}{m} & -\frac{\sin(\delta_f)}{m} & 0 & 0 \\
\frac{\cos(\delta_f)}{m} & \frac{\cos(\delta_f)}{m} & \frac{1}{m} & \frac{1}{m} \\
\frac{l_f\cos(\delta_f)+t_w\sin(\delta_f)}{I_z} & \frac{l_f\cos(\delta_f)-t_w\sin(\delta_f)}{I_z} & -\frac{l_r}{I_z} & -\frac{l_r}{I_z} \\
\hline
\multicolumn{4}{c}{\mathbf{0}_{4\times4}} \\
\hline
\multicolumn{4}{c}{\mathbf{0}_{4\times4}} \\
\hline
\multicolumn{4}{c}{-\frac{x_1}{\sigma}\cdot\mathbf{I}_{4\times4}}
\end{array}\right] \tag{28}
$$

$$
B_l = \begin{bmatrix} 0 & 0 & 0 & \frac{\mu_c r_c n i_f}{2I_w} & \frac{\mu_c r_c n i_f}{2I_w} & -\frac{\mu_c r_c n i_r}{2I_w} & -\frac{\mu_c r_c n i_r}{2I_w} & \mathbf{0}_{1\times4} & \mathbf{0}_{1\times4} \end{bmatrix}^T \tag{29}
$$

$$
E_l = \begin{bmatrix} 0 & 0 & 0 & -\frac{R_eR_r+T_{b1}}{I_w} & -\frac{R_eR_r+T_{b2}}{I_w} & \frac{T_t i_r}{2I_w}-\frac{R_eR_r+T_{b3}}{I_w} & \frac{T_t i_r}{2I_w}-\frac{R_eR_r+T_{b4}}{I_w} & \mathbf{0}_{1\times4} & \mathbf{0}_{1\times4} \end{bmatrix}^T \tag{30}
$$

Using $\mathbf{X}(k)$ and $\mathbf{U}(k)$ and removing terms that are not related with $\mathbf{U}(k)$, the cost function is compactly expressed as follows:

$$
\begin{aligned}
J\left(\mathbf{x}_k, \mathbf{U}(k)\right) =& \mathbf{X}(k)^T\bar{\mathbf{Q}}\mathbf{X}(k) + \mathbf{U}(k)^T\bar{\mathbf{R}}\mathbf{U}(k) \\
&- 2\mathbf{X}_d(k)^T\bar{\mathbf{Q}}\mathbf{X}(k)
\end{aligned} \tag{32}
$$

where

$$
\begin{aligned}
\bar{\mathbf{Q}} =& blockdiag[Q,\cdots,Q,P] \\
\bar{\mathbf{R}} =& blockdiag[R,\cdots,R] \\
\mathbf{X}_d(k) =& [\mathbf{x}_{d,k},\mathbf{x}_{d,k+1},\cdots,\mathbf{x}_{d,k+N}]^T
\end{aligned} \tag{33}
$$

Here, the state covariance matrix P of the last step has same value as Q. the The cost function used in the calculation of the optimal control input is affected by the values of matrices Q and R. However, the constant values of the matrices do not actively address the time-variable situation of the vehicle. By setting target errors to be included in the term of the matrices, the controller can be designed to respond more sensitively to the target error. The values of Q and R that were used in this study is defined as follows:

$$
\begin{aligned}
&Q = \begin{cases} diag\big[\{1+\max(|\gamma|-|\gamma_d|,0)\}\cdot 5.01\cdot 10^9 \\ \times \mathbf{1}_{[1\times14]}\big],\ \textit{if}\ |\gamma_d| > 0.035\ \&\ |\gamma| > |\gamma_d| \\ diag\big[(3.16\cdot 10\cdot \dfrac{\lambda_1+\lambda_2}{2}+1)\cdot 3.16\cdot 10^3\cdot \mathbf{1}_{[1\times14]}\big], \\ else \end{cases} \\
&R = 1
\end{aligned} \tag{34}
$$

Here $\mathbf{1}$ is the vector of which each component is 1. Substituting (31) into (32), the cost function is rewritten as follows:

$$
\begin{aligned}
J\left(\mathbf{x}_k, \mathbf{U}(k)\right) =& \left(L^x\mathbf{x}_k + L^u\mathbf{U}(k) + L^e\right)^T\bar{\mathbf{Q}}\left(L^x\mathbf{x}_k\right. \\
&\left. + L^u\mathbf{U}(k) + L^e\right) + \mathbf{U}(k)^T\bar{\mathbf{R}}\mathbf{U}(k) \\
&- 2\mathbf{X}_d(k)^T\bar{\mathbf{Q}}\left(L^x\mathbf{x}_k + L^u\mathbf{U}(k) + L^e\right)
\end{aligned} \tag{35}
$$

Dropping the terms that are not related with $\mathbf{U}(k)$, (35) is simplified as follows:

$$
\begin{aligned}
&J\left(\mathbf{x}_k, \mathbf{U}(k)\right) = \mathbf{U}(k)^T\left((L^u)^T\bar{\mathbf{Q}}L^u + \bar{\mathbf{R}}\right)\mathbf{U}(k) \\
&+ 2\left(\mathbf{x}_k^T(L^x)^T\bar{\mathbf{Q}}L^u + (L^e)^T\bar{\mathbf{Q}}L^u - \mathbf{X}_d(k)^T\bar{\mathbf{Q}}L^u\right)\mathbf{U}(k)
\end{aligned} \tag{36}
$$

Finally, the optimal control sequence that minimize the cost function (36) is calculated as follows:

$$
\begin{aligned}
\mathbf{U}(k) =& -\left((L^u)^T\bar{\mathbf{Q}}L^u + \bar{\mathbf{R}}\right)^{-1} \\
&\times \left(\mathbf{x}_k^T(L^x)^T\bar{\mathbf{Q}}L^u + (L^e)^T\bar{\mathbf{Q}}L^u - \mathbf{X}_d(k)^T\bar{\mathbf{Q}}L^u\right)^T
\end{aligned} \tag{37}
$$

Here, only the first component of the control input sequence (37) is used, because the sensor signal and estimation values are updated in every time step. Then, the final input command is determined by enveloping the input constraint (23).

VI. Experimental Setup

To validate the performance of the suggested controller, an experiment was conducted using a full-size AWD sedan. Fig. 2b shows the type of drivetrain used in this experiment. Fig. 4 is a block diagram of the proposed controller.

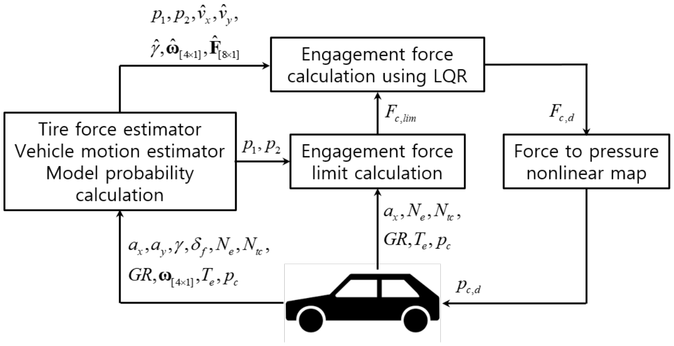

Fig. 4. Block diagram of the suggested AWD controller.

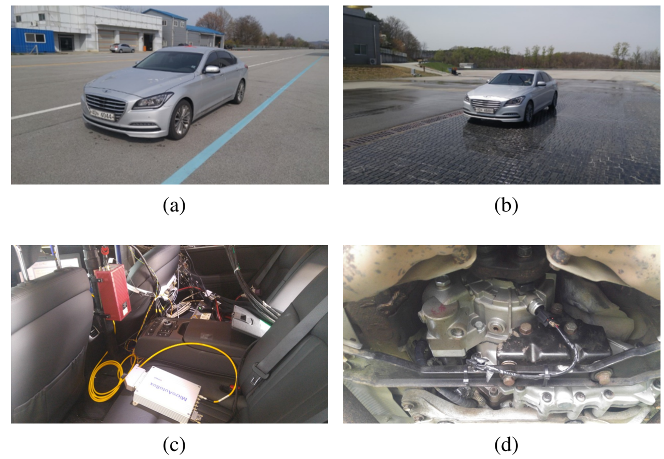

Fig. 5. Experimental setup and test environment of AWD vehicle. (a) Vehicle test on dry asphalt. (b) Vehicle test on a wet pebble road. (c) Upper level controller device and sensors. (d) Transfer case equipped in the vehicle.

TABLE I
VEHICLE SPECIFICATIONS AND TIRE MODELING PARAMETERS

Parameter	Value	Parameter	Value
l_f	$1.471m$	l_r	$1.539m$
h	0.61m	$2t_w$	1.63m
m	$2050kg$	I_z	$4200kg \cdot m^2$
I_w	$0.9kg \cdot m^2$	R_e	$0.368m$
R_r	0.015	i_f	3.916
i_r	3.909	C_1	$60913N/rad$
C_2	$-81456N/rad^2$	K_L	$108422N/m$
k_1	0.85	k_2	0.15

First, using the readily attainable vehicle CAN signals, i.e., $a_x, a_y, \gamma, \delta_f, \boldsymbol{\omega}_{[4\times1]}$, engine torque (T_e), engine RPM (N_e), torque converter RPM (N_{tc}), gear ratio (GR), and clutch engagement pressure (p_c) that were embedded in the private CAN, estimates of vehicle motions, tire forces, and the probabilities of lock-up and slipping states are calculated. Then, estimates of motions and tire forces are used to calculate the optimal control input. Probability values are used to calculate the engagement force limit. Fig. 5c shows the device for the upper level controller and an inertial measurement unit (IMU) measurement. An IMU was attached and used only for analysis. Then, a dSPACE MicroAutoBox device was used for data logging and the upper level controller. The lower level controller was designed to operate independently and to follow the desired pressure command with motor position and pressure as the sensor feedback. To verify the effectiveness of the suggested controller, a vehicle experiment was performed under various driving scenarios on the proving ground of the Korea Automotive Technology Institute. The sampling time was set at 5-ms. Considering both transient range determined by the tire relaxation length and computational capacity of real-time controller, prediction step was set to 8. Table I shows the numerical values of the vehicle parameters that were used in the controller. The hydraulic system of the transfer case was developed to have a maximum engagement pressure of 13 bar.

VII. EXPERIMENTAL RESULTS

A. Longitudinal Acceleration on Dry Asphalt

The first test of the experiment involved longitudinal acceleration without steering on dry asphalt. Figure 6 shows the experimental results. To keep the same input condition, the vehicle started to accelerate from the stopped state maintaining full throttle constantly. AWD vehicle with LQR controller was compared with 2WD, 4WD (fully lock-up state of transfer-case clutch), and AWD vehicle with the rule-based controller. For a strict comparison between model-based controller and rule-based one, experiments of AWD vehicle were conducted repetitively and representative values were used for analysis. Although the traction control system (TCS) was on, it was not activated in all cases. Figure 6a shows the longitudinal velocity. The black solid line is 2WD case. The red dotted line is AWD case with the suggested controller. The blue dash-dot line is AWD case with the rule-based controller, and the green dashed line is 4WD case. In the dry asphalt case, there were no big differences in longitudinal velocity depending on vehicle modes. However, the final velocity of the vehicle was slightly different in each case. Certainly, the final velocity was the lowest in the case of 2WD. The final velocity of AWD vehicle with the suggested controller was the fastest among all cases. This is because driving shaft resistance has a great effect when the vehicle is in a high gear, which causes 4WD vehicle not to maintain the optimal traction force. The final velocity of the AWD vehicle with the rule-based controller was slower than 4WD case, which proves that the control algorithm for a proper amount of engagement force and the disengagement timing is highly required for maximized performance of an AWD vehicle. Figure 6c shows the engagement force of the suggested controller (exp). The black solid line is the command. The blue dash-dot line is the fixed engagement force limit calculated from (21), and the red dotted line is the variable engagement force limit calculated from (23). With the LQR-based controller, it was verified that preemptive response appeared in the AWD system. More specifically, a certain amount of engagement force command

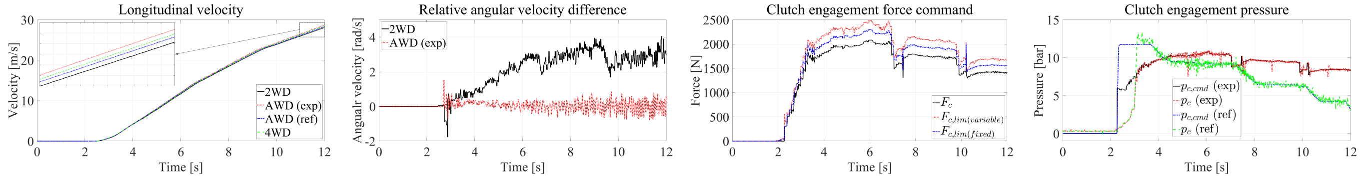

(a) (b) (c) (d)

Fig. 6. Acceleration on dry asphalt. (a) Longitudinal velocity. (b) Angular velocity difference between front and rear shaft (exp, 2WD). (c) Engagement force (exp). (d) Engagement pressure (exp, ref).

TABLE II
EXPERIMENTAL RESULT OF LONGITUDINAL ACCELERATION ON DRY ASPHALT DEPENDING ON VEHICLE MODES.

Type	Final v_x (m/s)
2WD	28.07
AWD (exp)	28.66
AWD (ref)	28.30
4WD	28.44

was generated from the initial moment of acceleration and then it continued to decrease slowly. In the dry asphalt case, engagement force was below both the fixed and the variable input constraint, which means input saturation didn't occur. Model probability was almost near lock-up state and persisted constantly because angular velocity difference was maintained within a certain range (see Figure 6b). Figure 6d shows the engagement pressure of both the model-based controller and the rule-based one. The black solid and red dotted lines are for the suggested one, and the blue dash-dot and green dashed lines are for rule-based one. Here, the engagement force of the rule-based controller reached its limit and then decreased gradually. Table II summarizes the experimental result of longitudinal acceleration on dry asphalt depending on vehicle modes.

B. Longitudinal Acceleration on Wet Pebble Road

The second test of the experiment involved longitudinal acceleration without steering on a wet pebble road (see Figure 5b). Figure 7 shows the experimental results. All other conditions of vehicle inputs were the same as in the first test. Figure 7a shows the longitudinal velocity. In the wet pebble road case, there were big differences in longitudinal velocity between 2WD case and other cases. The final velocity of AWD vehicle with the suggested controller was faster than the rule-based one. However, AWD vehicle with the suggested controller was slower than 4WD vehicle, because both the front and rear wheels still had the opportunity to secure optimal traction force on wet pebble road for an extended amount of time. Figure 7c shows TCS activation time, and Figure 7d shows the requested engine torque commanded from TCS. TCS activation time was fastest in 2WD and slowest in 4WD cases. Albeit not as much as 4WD, the suggested controller could delay TCS activation time, as compared to 2WD vehicle. Although there was no significant difference of TCS activation time between the suggested controller and the rule-based one, the suggested controller could reduce the intervention amount of TCS. Figure 7e shows the engagement force of the suggested controller (exp). Figure 7f shows the engagement pressure of both model-based controller and rule-based one. Due to the thermal safety algorithm of lower level controller, clutch engagement pressure was restricted to 13 bar, which didn't generate enough engagement force calculated by controller (see $t = 3 - 3.3s, t = 3.6 - 5s$, and $t = 7.5 - 8.4s$ of Figure 7f). At the initial stage of vehicle acceleration on wet pebble road, response of LQR-based controller and model probability were similar with those of dry asphalt case. However, despite the strong engagement force of transfer case clutch, there appeared higher angular velocity difference between front and rear shaft after $t = 2s$ than the dry asphalt case, which is due to surface irregularities (see Figure 7b). And model probability was almost slipping state. Therefore, the difference between the fixed input constraint and the variable one became larger drastically (see $t = 3s$ of Figure 7e). With the variable input constraint, the range of the engagement pressure limit was expanded more than the dry asphalt case, which contributed the vehicle with the suggested controller to have better acceleration performance than that with the rule-based one, by reducing wheel slip ratio as fast as possible. Also, In contrast with the dry asphalt case, the engagement force command of the suggested controller lasted longer due to the increase of cost function Q which includes wheel slip ratio term (see the difference of red dotted line between Figure 6b and Figure 7b), which proves that the model-based controller effectively differentiated the road conditions. In the wet pebble road case, engagement force was upper than the fixed input constraint and slightly lower than the variable input constraint during most of time, but saturation occurred intermittently with the decrement of relative angular velocity difference (see $t = 6.5 - 7.2s$ and $t = 11.7{-}11.9s$ of Figure 7b and 7e). Table III summarizes the experimental result of longitudinal acceleration on wet pebble road depending on vehicle modes.

C. Acceleration during Steady-State Cornering

The third test of the experiment involved acceleration during steady state cornering. Figure 8 shows the experimental results. Here, the vehicle started to accelerate, slowly increasing throttle to reach a certain velocity while keeping a constant turning radius (see Figure 8a, 8c, and 8h). To prevent the intervention of other vehicle dynamics controllers, the test was performed with TCS and ESC off. Since steering wheel angle values were

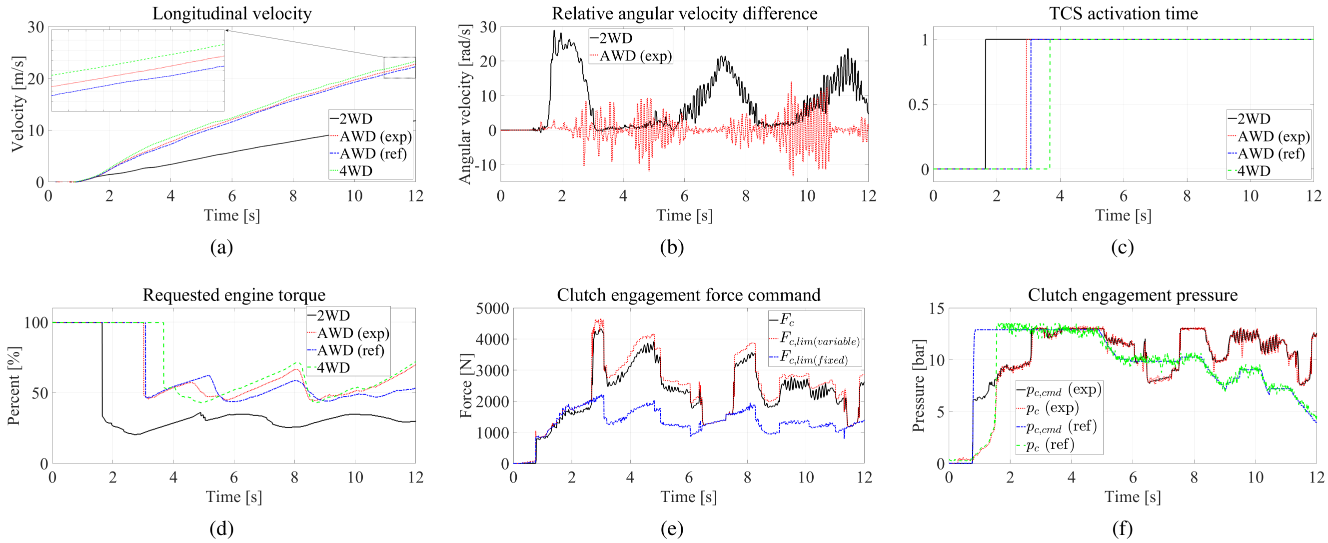

Fig. 7. Acceleration on a wet pebble road. (a) Longitudinal velocity. (b) Angular velocity difference between front and rear shaft (exp, 2WD). (c) TCS activation time. (d) Requested engine torque. (e) Engagement force (exp). (f) Engagement pressure (exp, ref).

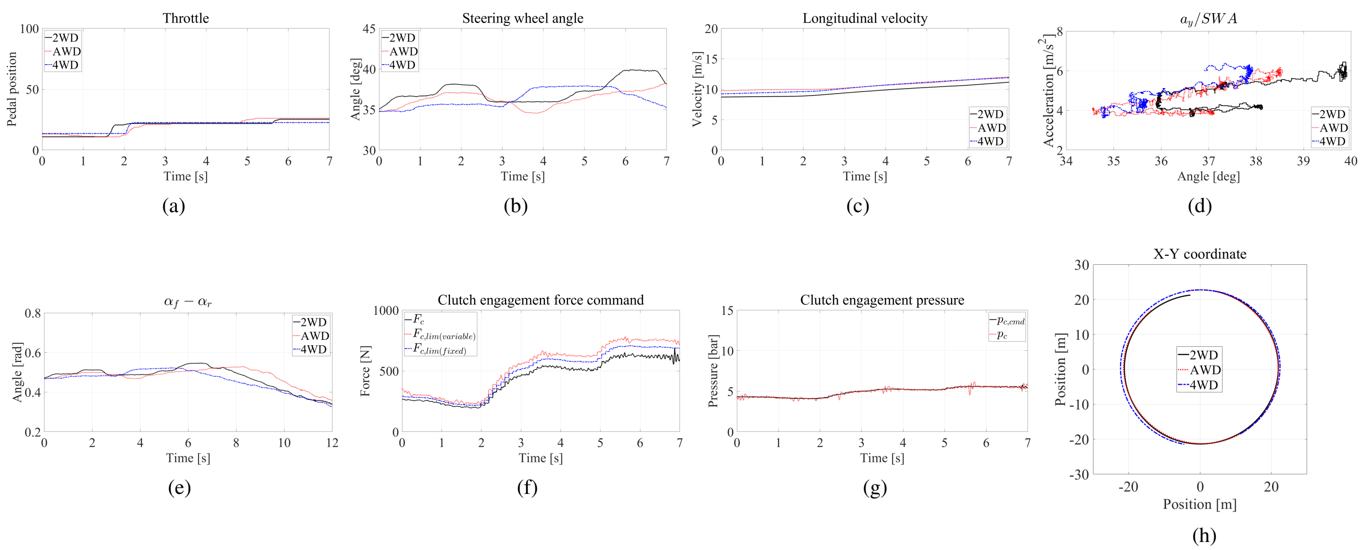

Fig. 8. Acceleration during steady state cornering. (a) Throttle. (b) Steering wheel angle. (c) Longitudinal velocity. (d) Lateral acceleration vs. steering wheel angle. (e) Sideslip angle difference between front and rear wheel. (f) Engagement force. (g) Engagement pressure. (h) X-Y coordinate.

TABLE III
EXPERIMENTAL RESULT OF LONGITUDINAL ACCELERATION ON WET PEBBLE ROAD DEPENDING ON VEHICLE MODES.

Type	Final v_x (m/s)	TCS time (s)	Req. tq. red. $(\%)$
2WD	11.87	1.67	29.91
AWD (exp)	22.70	2.95	53.38
AWD (ref)	22.21	3.08	51.01
4WD	23.28	3.69	54.75

all different in each case (see Figure 8b), lateral acceleration vs. steering wheel angle was compared instead of yaw rate. There appeared to be a distinguishable difference in the lateral acceleration vs. steering wheel angle, depending on the vehicle modes. At the initial stage of throttle input, where the driver starts maneuvering to find another steady-state cornering condition, AWD vehicle with the suggested controller could achieve same lateral acceleration without increasing steering wheel angle more than 2WD (see Figure 8d). In case of sideslip angle difference between front wheel and rear wheel, any significant differences were not found between the vehicle modes (see Figure 8e). In AWD vehicle, the engagement force command steadily increased as the vehicle velocity increased (see Figure 8f). 4WD and AWD vehicle showed no much big difference which verifies that the suggested AWD controller achieved similar behavior as 4WD with less control effort.

D. Acceleration during Slow Ramp Steer

The fourth test of the experiment involved acceleration with ramp steering. Figure 9 shows the experimental results. Here,

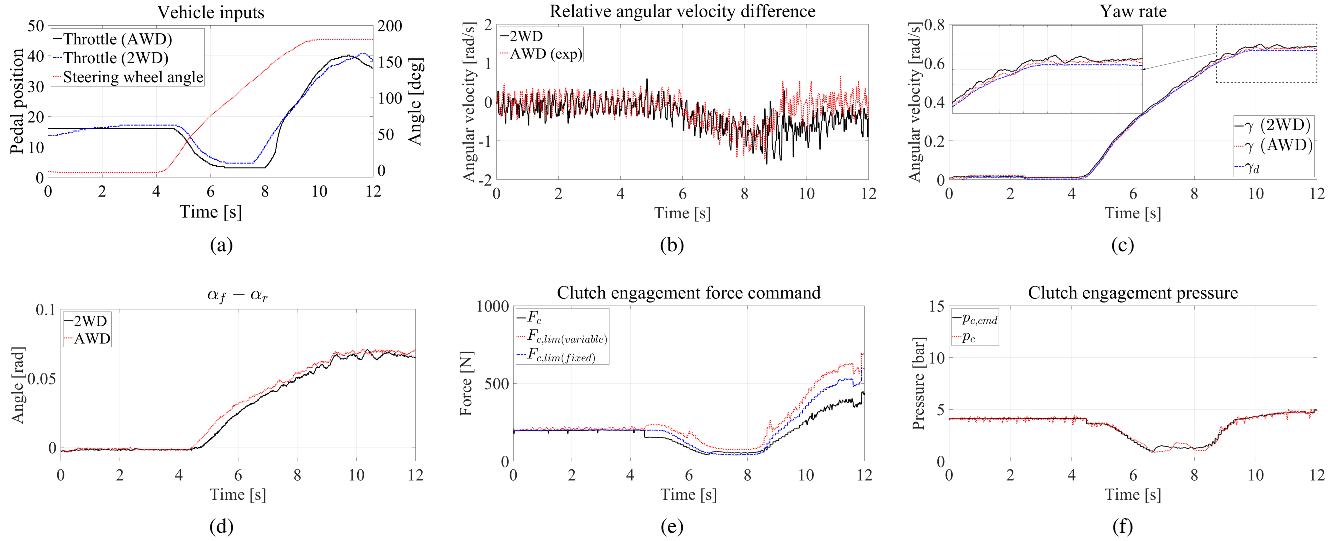

Fig. 9. Acceleration during slow ramp steer. (a) Vehicle inputs. (b) Angular velocity difference between front and rear shaft. (c) Yaw rate. (d) Sideslip angle difference between front and rear wheel. (e) Engagement force. (f) Engagement pressure.

the vehicle started to accelerate while the steering wheel angle was increased from 0 to 180 deg. (see Figure 9a). Using a steering robot, exactly the same steering wheel angle profile was applied in both cases. There was a slight difference in yaw rate between 2WD vehicle and AWD vehicle with the suggested controller. In detail, the yaw rate of AWD vehicle was lower than that of 2WD vehicle and more consistent with γ_d (see Figure 9c). The difference between 2WD and AWD vehicle was more pronounced in the sideslip angle difference between front and rear wheels. Compared with 2WD vehicle, AWD vehicle showed much more sideslip angle difference, which means that AWD vehicle had more understeering behavior than 2WD vehicle did (see Figure 9d). Figure 9e and 9f are the engagement force and engagement pressure of the suggested controller, respectively. Before steering, AWD vehicle was near lock-up state. However, model probability of lock-up state decreased as soon as steering event occurs because the angular velocity difference between front and rear shaft instantaneously increased (see $t = 5 - 9s$ of Figure 9b).

E. Climbing Beam-Roller

The fifth test of the experiment was a climbing beam-roller test. Here, the role of the transfer case was paramount, because the front wheel was hung on a rectangular beam and the rear wheel was on a roller. Then, the vehicle started to accelerate, slowly increasing the throttle (see Figure 10a). Although transfer case clutch was not fully locked-up, AWD vehicle with the suggested controller could pass the beam-roller and escaping performance was not much different from 4WD vehicle (see Figure 10b and Figure 10c). Figure 10d and 10e are the engagement force and engagement pressure of the suggested controller, respectively. Here, the engagement force preemptively increased to provide traction to the front wheels along with the increase of the throttle amount.

VIII. Conclusion

In this paper, a model-based controller for an AWD vehicle was proposed. With the novel AWD vehicle dynamic model that represents the direct relationship between the states and control inputs, the LQR method, which can calculate the optimal control input, was used for the advanced AWD controller design. Especially, the variable clutch engagement force constraint which arises from the current vehicle dynamic state-dependent transfercase characteristics was systematically considered and applied as an upper limit for optimized AWD vehicle performance regardless of road conditions. In the case of acceleration in the longitudinal direction on both dry asphalt and wet pebble road, the suggested model-based controller showed better acceleration performance than the rule-based one did. Also, the model-based controller was proved to reduce the intervention amount of TCS compared to the rule-based one on wet pebble road. Furthermore, it was verified that AWD vehicle could contribute to enhance the lateral response, i.e., maintaining higher lateral acceleration over steering wheel angle in the acceleration during steady-state cornering and maintaining more consistent understeering response in the acceleration during slow ramp steering than 2WD vehicle. It was also noteworthy that the suggested controller could deal with various driving scenarios and road conditions without having severely oscillated or lagged control input behavior. The suggested vehicle dynamics model can be expanded to a side-to-side torque vectoring system, such as an electronic limited slip differential (e-LSD), then the suggested control scheme can be properly extended for a unified vehicle dynamics controller for AWD and e-LSD system ultimately.

Acknowledgment

The authors would like to thank C. W. Moon, D. Y. Kim and B. J. Pyun of Korea Automotive Technology Institute for their efforts in carrying out experiments. This paper has its origin in the project titled by ”Development of 1,300Nm

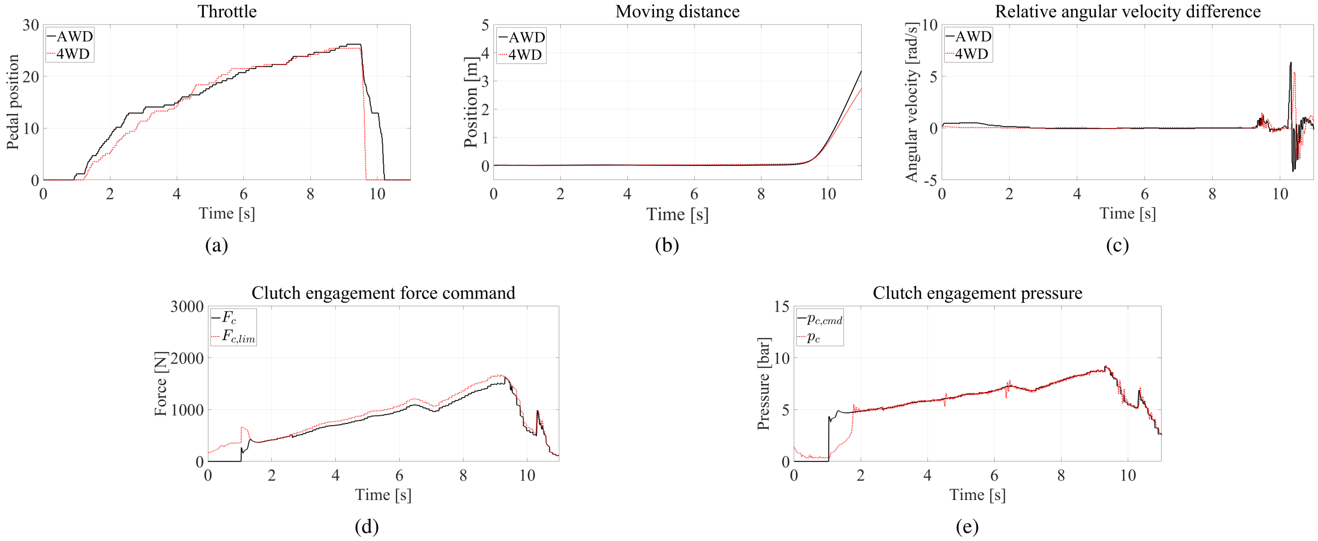

Fig. 10. Climbing beam-roller. (a) Throttle. (b) Moving distance. (c) Angular velocity difference between front and rear shaft. (d) Engagement force. (e) Engagement pressure.

Electro-Hydraulic AWD Modularization System and Control Technology to Improve Driving Force and Safety", without which this paper could not have been completed.

References

[1] S. B. Choi, "Antilock brake system with a continuous wheel slip control to maximize the braking performance and the ride quality," *IEEE Transactions on Control Systems Technology*, vol. 16, no. 5, pp. 996–1003, Sep. 2008.

[2] J. Yoon, W. Cho, B. Koo, and K. Yi, "Unified chassis control for rollover prevention and lateral stability," *IEEE Transactions on Vehicular Technology*, vol. 58, no. 2, pp. 596–609, Feb. 2009.

[3] M. Choi and S. B. Choi, "Mpc for vehicle lateral stability via differential braking and active front steering considering practical aspects," *Proc IMechE Part D: J Automobile Engineering*, vol. 230, no. 4, pp. 459–469, 2016.

[4] R. C. Williams, "4wd-awd market trends in vehicles and technology differences and similarities, from 1997 to 2004 primarily in the us market, and also some global comparisons," in *SAE Technical Paper*, no. 2006-01-0822, Apr. 2006.

[5] H. Kim, S. Lee, and J. K. Hedrick, "Active yaw control for handling performance improvement by using traction force," *International Journal of Automotive Technology*, vol. 16, no. 3, pp. 457–464, Jun. 2015.

[6] R. P. Osborn and T. Shim, "Independent control of all-wheel-drive torque distribution," *Vehicle System Dynamics*, vol. 44, no. 7, pp. 529–546, 2006.

[7] M. Croft-White and M. Harrison, "Study of torque vectoring for all-wheel-drive vehicles," *Vehicle System Dynamics*, vol. 44, no. sup1, pp. 313–320, 2006.

[8] K. Han, M. Choi, B. Lee, and S. B. Choi, "Development of a traction control system using a special type of sliding mode controller for hybrid 4wd vehicles," *IEEE Transactions on Vehicular Technology*, vol. 67, no. 1, pp. 264–274, Jan. 2018.

[9] M. Choi and S. B. Choi, "Model predictive control for vehicle yaw stability with practical concerns," *IEEE Transactions on Vehicular Technology*, vol. 63, no. 8, pp. 3539–3548, Oct. 2014.

[10] K. Nam, H. Fujimoto, and Y. Hori, "Lateral stability control of in-wheel-motor-driven electric vehicles based on sideslip angle estimation using lateral tire force sensors," *IEEE Transactions on Vehicular Technology*, vol. 61, no. 5, pp. 1972–1985, Jun. 2012.

[11] W. Cho, J. Yoon, S. Yim, B. Koo, and K. Yi, "Estimation of tire forces for application to vehicle stability control," *IEEE Transactions on Vehicular Technology*, vol. 59, no. 2, pp. 638–649, Feb. 2010.

[12] W. Cho, J. Choi, C. Kim, S. Choi, and K. Yi, "Unified chassis control for the improvement of agility, maneuverability, and lateral stability," *IEEE Transactions on Vehicular Technology*, vol. 61, no. 3, pp. 1008–1020, Mar. 2012.

[13] J. Yi, J. Li, J. Lu, and Z. Liu, "On the stability and agility of aggressive vehicle maneuvers: A pendulum-turn maneuver example," *IEEE Transactions on Control Systems Technology*, vol. 20, no. 3, pp. 663–676, May 2012.

[14] K.-S. Kim and F. Jabbari, "Using scales in the multiobjective approach," *IEEE Transactions on Automatic Control*, vol. 45, no. 5, pp. 973–977, May 2000.

[15] C. B. A. Eduardo F. Camacho, *Model Predictive Control*, 2nd ed., ser. Automotive engineering. Springer-Verlag London, 2007.

[16] F. Borrelli, A. Bemporad, and M. Morari, *Predictive Control for Linear and Hybrid Systems*. Cambridge University Press, 2017.

[17] A. Bemporad, M. Morari, V. Dua, and E. N. Pistikopoulos, "The explicit linear quadratic regulator for constrained systems," *Automatica*, vol. 38, no. 1, pp. 3 – 20, 2002.

[18] M. Jalali, A. Khajepour, S. ken Chen, and B. Litkouhi, "Handling delays in yaw rate control of electric vehicles using model predictive control with experimental verification," *ASME J Dyn Sys Meas Control*, vol. 139, no. 12, 2017.

[19] F. Borrelli, A. Bemporad, M. Fodor, and D. Hrovat, "An mpc/hybrid system approach to traction control," *IEEE Transactions on Control Systems Technology*, vol. 14, no. 3, pp. 541–552, May 2006.

[20] C. E. Beal and J. C. Gerdes, "Model predictive control for vehicle stabilization at the limits of handling," *IEEE Transactions on Control Systems Technology*, vol. 21, no. 4, pp. 1258–1269, Jul. 2013.

[21] S. D. Cairano, H. E. Tseng, D. Bernardini, and A. Bemporad, "Vehicle yaw stability control by coordinated active front steering and differential braking in the tire sideslip angles domain," *IEEE Transactions on Control Systems Technology*, vol. 21, no. 4, pp. 1236–1248, Jul. 2013.

[22] J. Suh, K. Yi, J. Jung, K. Lee, H. Chong, and B. Ko, "Design and evaluation of a model predictive vehicle control algorithm for automated driving using a vehicle traffic simulator," *Control Engineering Practice*, vol. 51, pp. 92 – 107, 2016.

[23] H. J. Ferreau, C. Kirches, A. Potschka, H. G. Bock, and M. Diehl, "qpoases: a parametric active-set algorithm for quadratic programming," *Mathematical Programming Computation*, vol. 6, no. 4, pp. 327–363, Dec. 2014.

[24] J. Mattingley and S. Boyd, "Automatic code generation for real-time convex optimization," in *Convex Optimization in Signal Processing and Communications*, D. P. Palomar and Y. C. Eldar, Eds. Cambridge University Press, 2009, pp. 1—41.

[25] R. Rajamani, *Vehicle Dynamics and Control*, 2nd ed., F. F. Ling, Ed. New York, USA: Springer, 2012.

[26] E. Lee, H. Jung, and S. Choi, "Tire lateral force estimation using kalman filter," *International Journal of Automotive Technology*, vol. 19, no. 4, pp. 669–676, Aug. 2018.

[27] J. Kim, "Identification of lateral tyre force dynamics using an extended kalman filter from experimental road test data," *Control Engineering Practice*, vol. 17, no. 3, pp. 357–367, Mar. 2009.

[28] K. Nam, S. Oh, H. Fujimoto, and Y. Hori, "Estimation of sideslip and roll angles of electric vehicles using lateral tire force sensors through rls and kalman filter approaches," *IEEE Transactions on Industrial Electronics*, vol. 60, no. 3, pp. 988–1000, Mar. 2013.

[29] M. Choi, J. J. Oh, and S. B. Choi, "Linearized recursive least squares methods for real-time identification of tire road friction coefficient," *IEEE Transactions on Vehicular Technology*, vol. 62, no. 7, pp. 2906–2918, Sep. 2013.

[30] H. Pacejka, *Tire and Vehicle Dynamics*, ser. Automotive engineering. Butterworth-Heinemann, 2006.

[31] M. Burckhardt, *Fahrwerktechnik, Radschlupf-Regelsysteme*. Würzburg: Vogel Fachbuch, 1993.

[32] H. Jung and S. B. Choi, "Real-time individual tire force estimation for an all-wheel drive vehicle," *IEEE Transactions on Vehicular Technology*, vol. 67, no. 4, pp. 2934–2944, Apr. 2018.

[33] K. Han, E. Lee, M. Choi, and S. B. Choi, "Adaptive scheme for the real-time estimation of tire-road friction coefficient and vehicle velocity," *IEEE/ASME Transactions on Mechatronics*, vol. 22, no. 4, pp. 1508–1518, Aug. 2017.

[34] J. J. Oh and S. B. Choi, "Vehicle velocity observer design using 6-d imu and multiple-observer approach," *IEEE Transactions on Intelligent Transportation Systems*, vol. 13, no. 4, pp. 1865–1879, Dec. 2012.

Hojin Jung received the B.S. and M.S. degrees in mechanical engineering from the Korea Advanced Institute of Science and Technology (KAIST), Daejeon, Korea, in 2012 and 2014, respectively, where he is currently working toward the Ph.D. degree in mechanical engineering. His research interests include vehicle dynamics and control, vehicle system modeling and simulation, and control theory.

Dohyun Jung received B.S. degree from Seoul National University, Seoul, Korea in 1992 and received the M.S. and Ph.D. degree in mechanical engineering from Korea Advanced Institute of Science and Technology (KAIST), Daejeon, Korea, in 1994 and 2001, respectively. He is currently a vice president of Convergence Systems R&D Division at Korea Automotive Technology Institute (KATECH).

Seibum B. Choi received the B.S. degree in mechanical engineering from Seoul National University, Seoul, South Korea, in 1985, the M.S. degree in mechanical engineering from the Korea Advanced Institute of Science and Technology (KAIST), Daejeon, South Korea, in 1987, and the Ph.D. degree in controls from the University of California, Berkeley, CA, USA, in 1993. From 1993 to 1997, he was with the Institute of Transportation Studies, University of California, working on the development of automated vehicle control systems. Through 2006, he was with TRW, Livonia, MI, USA, where he worked on the development of advanced vehicle control systems. Since 2006, he has been with the Faculty of the Mechanical Engineering Department, KAIST. His research interests include fuel-saving technology, vehicle dynamics and control, and active safety systems. He is a Member of the American Society of Mechanical Engineers, the Society of Automotive Engineers, and the Korean Society of Automotive Engineers.